DIFFERENTIAL CROSS SECTIONS OF THE NEUTRAL PION PHOTOPRODUCTION FROM HYDROGEN IN THE ENERGY RANGE BETWEEN 390 AND 975 MeV

By

Masakazu YOSHIOKA*

Department of Physics, Faculty of Science, Kyoto University

ABSTRACT

The differential cross sections of the reaction $\gamma p \rightarrow \pi^\circ p$ have been measured at the photon energies between 390 MeV and 975 MeV with the energy steps of 20 MeV or 25 MeV. The angular range covered between 15° and 130° in the center of mass system. Recoil protons were detected with a magnetic spectrometer and a photon decayed from a π°-meson was also detected in coincidence with a photon detector at the angles from 50° to 130°. Two photons from a π°-meson were detected by a pair of photon detectors at the angles of 15°, 35° and 50°. The experimental results are compared with the recent partial wave analyses.

Chapter I. Introduction

Over the last twenty years many measurements of the differential cross sections $\sigma(\theta)$ on the single pion photoproduction processes have been performed in the resonance region to investigate the electromagnetic properties of the nucleon resonances and the behaviour of the non-resonant terms. As is well known, there are four invariant complex amplitudes in the single pion photoproduction process. Therefore, we need at least seven different experimental measurements to determine the photoproduction amplitudes at one kinematical point (incident photon energy $[K]$ and pion angle in the center of mass system $[\theta_\pi^{cm}]$). Many experimental efforts have been devoted to measure the spin dependent parameters such as a polarization of the recoil nucleon $P(\theta)$, a polarized photon asymmetry $\Sigma(\theta)$ and a polarized target asymmetry $T(\theta)$, in the last ten years. Recently, double spin correlation parameters were measured using the polarized photon and the polarized target[1].

The gross features of the above experimental results[2] are well explained by the recent phenomenological analyses. Metcalf and Walker (MW)[3],[4] decomposed the photoproduction amplitudes into three parts; an electric Born term, a resonant term described with a Breit-Winger formula and an additional "background" term in the lower partial waves. They used a considerable amount of data and determined the electromagnetic couplings of the nucleon resonance below 2 GeV. Feller et al. (NAGOYA)[5] fitted the data at a photon energy below 1.2 GeV specially emphasizing their polarization measurement of $T(\theta)$[6]. Their model was essentially the same as

---

* Now at the Institute for Nuclear Study, University of Tokyo

the one by MW. Knies-Moorhause-Oberlack (KMO)[7], Moorhause-Oberlack-Rosenfeld (MOR)[8] and Devenish-Lyth-Rankin (DLR)[9] used the fixed-t dispersion relations in their analyses. They calculated the real part of amplitudes from the imaginary part of amplitudes assuming that the imaginary part is dominated at the resonance. On the other hand, there are some theoretical predictions on the photon couplings basing on a simple quark model[10]~[12]. These predictions show a fairly good agreement with above analyses only on the dominant resonances such as $P_{33}(1236)$, $D_{13}(1513)$ and $F_{15}(1688)$.

The number of data on single pion photoproduction is not so abandant in comparison with those by nucleon scattering experiments and there are still some discrepancies among the experimental results of the photoproduction from different laboratories. Fig. 1 shows the summary of the existing experimental data on the differential cross section for the reaction $\gamma p \rightarrow \pi^{\circ}p$. The aim of the present work is to offer accurate data of differential cross sections for the reaction $\gamma p \rightarrow \pi^{\circ}p$ over a wide angular range in the incident photon energy range between 390 and 975 MeV.
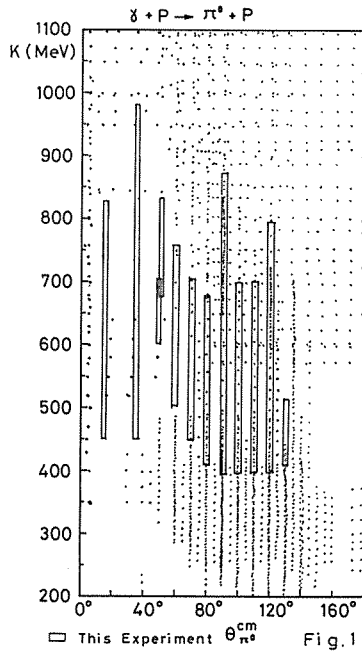

Fig. 1. Summary of the existing experimental data for the reaction $\gamma p \rightarrow \pi^{\circ}p$ below 1.1 GeV.

In this energy region, there are some interferences between the tail of the first resonance [$P_{33}(1236)$] and the second resonances dominated by $D_{13}(1520)$ and other small resonances such as $P_{11}(1470)$ and $S_{11}(1535)$. It is promising to study the reaction $\gamma p \rightarrow \pi^{\circ}p$ for the investigation on the small resonant amplitudes because of the relatively small contribution of the Born term comparing with the reaction $\gamma p \rightarrow \pi^{+}n$.

There are few systematic experiments on the cross sections for the reaction $\gamma p \rightarrow \pi^{\circ}p$ in the energy range between 450 and 600 MeV covering a wide angular range with the exception of Dougan et al.[13],[14]. In their experiment, only recoil protons

were detected with a range telescope. In the present work a recoil proton was detected with a magnetic spectrometer having a large momentum acceptance and one of the photons decayed from a π°-meson was also detected with the photon detector in coincidence in the angular range from 50° to 130°. Moreover, the differential cross sections of this process at forward angles ($\theta_{\pi^\circ}^{cm} \to 50°$) have been measured simultaneously with a π°-detector consisting of a pair of photon detectors. Experimental equipments and procedure are described in Chapter II. The reduction of differential cross section is stated in Chapter III. Experimental results and discussions are given in Chapter IV and V, respectively.

Chapter II.   Experimental Equipments and Procedure

II-1.   *General description*

The experimental layout is shown in Fig. 2. A photon beam from the 1.3 GeV electron synchrotron at Institute for Nuclear Study, University of Tokyo, was incidented on a liquid hydrogen target. Recoil protons were detected with the magnetic spectrometer (proton arm) and a photon decayed from a π°-meson was detected with the photon detector (gamma arm) in coincidence. These detection systems were mounted on rotatable platforms. The π°-detector for the measurement at the forward angle was also mounted on an another platform. A pair spectrometer was set at the upstream of the beam line and was used to calibrate the photon detector. All informations were stored in a computer system and analysed in a real time.
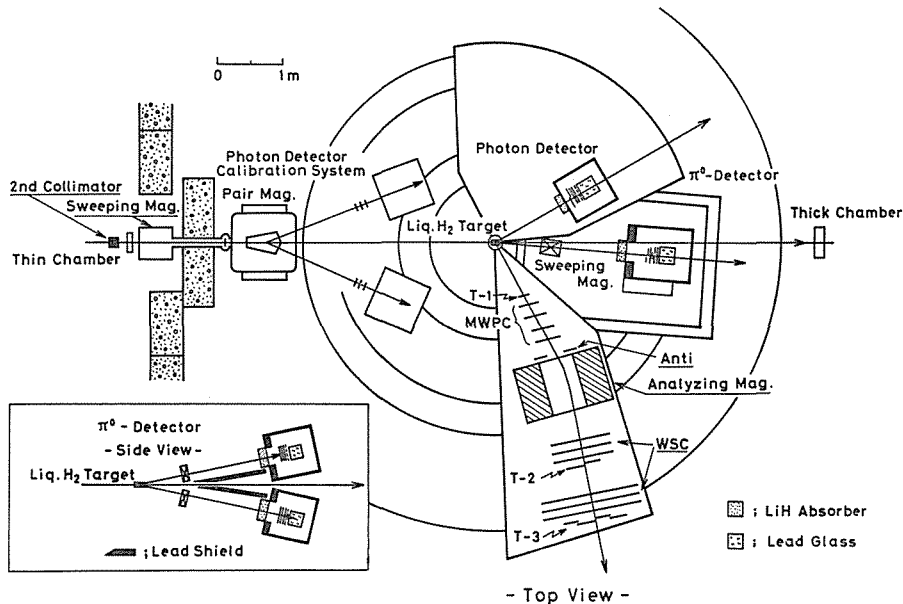

Fig. 2.   Schematic view of the experimental arrangement of the present experiment.

II-2.   *Photon beam and the liquid hydrogen target*

Electrons in the synchrotron were striked onto a platinum radiator of 50 μm thick to produce the bremsstrahlung after accelerated near the maximum energy.

The spill of the bremsstrahlung was kept to be about 4 m sec to reduce the rate of a chance coincidence throughout the experiment. The resulting bremsstrahlung was defined by two lead collimators to give a beam spot of 30 mm in diameter at the target position. A sweeping magnet was placed behind each collimator to reject charged particles in the photon beam. The intensity of the photon beam was monitored with a thick walled ionization chamber which was calibrated with a Faraday cup using extracted electron beam[15]. The typical value of the beam intencity was 1.5×10^9 equivalent quanta per second. A thin walled ionization chamber was also used as a supplementary monitor for the beam intensity. Scintillation counter telescopes in the pair spectrometer was used to monitor the beam condition.

The container of liquid hydrogen was a cylindrical shape of 106.5 mm length and 40.6 mm diameter made of Mylar and placed with its axis along the bremsstrahlung. The thickness of the cylindrical wall was 125 μm and that of the walls of both ends across the bremsstrahlung beam was 75 μm. The container was put in a vacuum vessel whose window was made of Mylar of 250 μm thick.

II-3. *Magnetic spectrometer (proton arm)*

Recoil protons were detected with the magnetic spectrometer[16] which consisted of four planes of a multiwire proportional chamber (MWPC #1~#4)[17], six planes of a multiwire spark chamber (WSC #1~#6)[18], an analysing magnet (Spark Chamber Magnet) and scintillation counters (T1, T2, T3 and ANTI), as shown in Fig. 3. MWPC and WSC determined the trajectory of the charged particle before and behind the magnet, respectively. The momentum of the particle was calculated from the trajectories and the magnetic field of the analysing magnet. The recoil proton was identified by the method as described afterward (II-5). The momentum of the
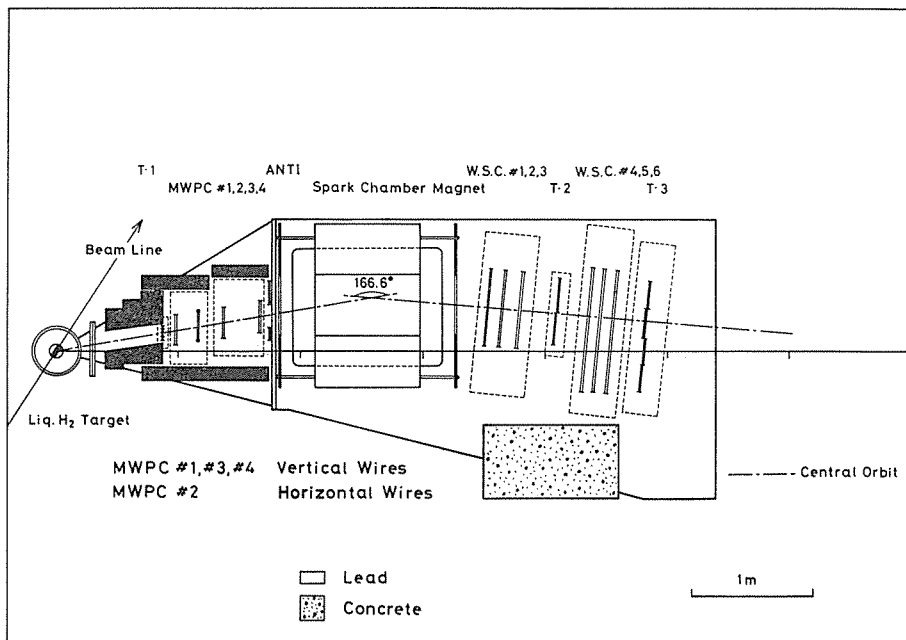

Fig. 3.   Magnetic spectrometer for the measurement of the recoil protons.

recoil proton in the present experiment ranged from 330 to 920 MeV/c. The momentum resolution calculated by the Monte Carlo method was 1.3% above 700 MeV/c and 6.0~1.3% between 330 and 700 MeV/c. The momentum acceptance ranged from 100 to 400 MeV/c and the typical angular acceptance was 3.7 msr.

(a) MWPC

The construction of MWPC is shown in Fig. 4. The basic design parameters were similar to those of Charpak et al.[19]. The dimension of the useful area was 280×280 mm². Two cathode planes were installed both sides of the anode plane. The gap between the anode and cathode plane was 6 mm. The cathode plane consisted of stainless steel wire of 100 μm in diameter with 1 mm spacing. The anode plane was consisted of gold plated tungsten wire of 29 μm in diameter with 2 mm spacing. Windows of each chamber were made of Mylar of 125 μm thick. Frames of each chamber were made of epoxy fiber glass. The anode plane was connected to the ground potential and a constant high voltage of 5.05 kV was supplied to the cathode plane. Anode wires were connected to the amplifier card. The mixing gas of 66% Argon, 33% isobutane and 1% Freon was continuously flowed to each chamber. The signal from the anode wire was amplified and encoded, then transferred to a small computer of TOSBAC–40 through CAMAC modules. The gate width to read out the data was chosen to be 100 n sec to achieve a high detection efficiency and a small background.

MWPC #1, #3 and #4 were used to read the vertical coordinate and #2 was used for the horizontal coordinate.
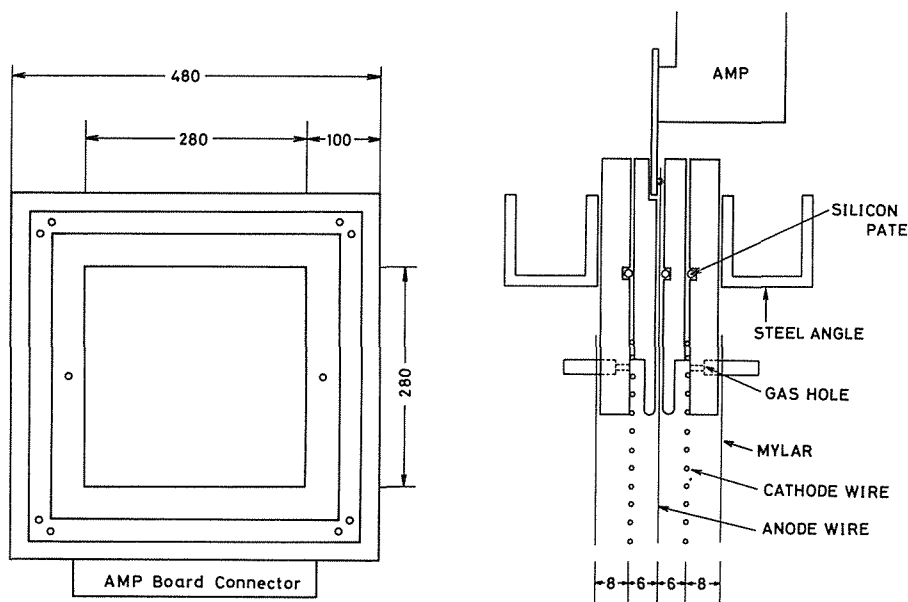

Fig. 4. Construction of the multiwire proportional chamber.

(b) WSC

The construction and dimension of WSC are shown in Fig. 5. A gap of the chamber was 8 mm and the useful area was 370×650 mm² (#1~#3) and 660×1040 mm² (#4~6#). Both plates of chambers were made of stainless steel wire of 100 μm

in diameter with 1 mm spacing. Windows of chambers were made of Mylar of 125 μm thick and frames were made of the same material as MWPC. Nelium gas were continuously flowed after mixing of Helium. The mixing gas was 67% Helium and 33% Neon. A clearing field of 80 Volt was applied to make the memory time short. High voltage pulse of 5~6 kV and 1 μ sec was generated by a Thyratron[20] which was triggered by a Krytron pulser. The total delay time of high voltage pulses after the passage of particles through the chamber was 1 μ sec.

The spark position was determined by the magnetostrictive delay line read out system which consisted of a magnetostrictive delay line, front and back fiducial wires, pick up coils, amplifiers, zero-crossing discriminators, a clock generator (20 MHz), interval scalers and a WSC controller.

	EFFECTIVE AREA		C cm	D cm	GAP cm	X (cm) F·FID-B·FID	Y (cm) F·FID-B·FID	Wire angle
	A cm	B cm						
#1	65	37	100	62	0.8	95	58	10°
#2	65	37	100	62	0.8	95	58	-10°
#3	65	37	100	62	0.8	95	58	0°
#4	104	66	160	100	0.8	148	90	-10°
#5	104	66	160	100	0.8	148	90	10°
#6	104	66	160	100	0.8	148	90	0°

F FID : FRONT FIDUCIAL
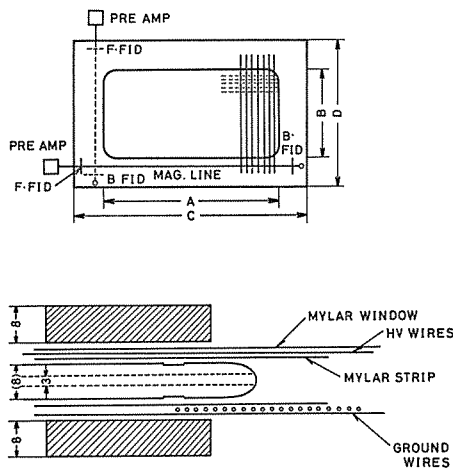B FID : BACK FIDUCIAL

Fig. 5. Dimension and construction of the multiwire spark chamber.

(c) Analysing magnet

An analysing magnet with a maximum field strength of 7.03 kG were used to measure the momentum of protons. The magnetic field was measured by the NMR method before and after the experiment. The field distribution in the useful volume of the magnet was also measured by the rotating coil method. The aperture of the magnet was 250 mm high and 50 mm wide, and the effective field length was 1016 mm.

(d) Scintillation counter

Four sets of scintillation counters were used to trigger the proton arm. T1 and ANTI were placed in front of the analysing magnet and T2 and T3 were placed behind the magnet. T1 consisted of four scintillation counters. The dimension of each scintillator was $30 \times 35 \times 3$ mm^3 (width $\times$ height $\times$ thickness). ANTI consisting of

two scintillation counters $(200 \times 250 \times 10 \text{ mm}^3)$ were placed in front of the magnet to restrict the acceptance. T2 consisted of two scintillation counters $(280 \times 280 \times 3 \text{ mm}^3)$ and T3 consisted of four scintillation counters $(170 \times 440 \times 6 \text{ mm}^3)$. Scintillators of T1, T2 and ANTI were viewed by photomultipliers from one side and those of T3 were viewed by photomultipliers from both sides. A light emission diode was connected to each photomultiplier to monitor the performance of the scintillation counter.

II–4. *Photon detector (gamma arm)*

(a) Construction

A construction of the photon detector[21] is shown in Fig. 6. The photons from the π° mesons were converted into electrons and positrons with a lead plate of 5.8 mm thick after passing through a lead collimator, a Lithium hydrate (LiH) absorber and veto counters. The hodoscope array of 20×20 placed right behind of the lead converter determined the conversion position of the photons. Then, the lead glass Čerenkov counter absorbed the total energy of converted electrons and positrons.

The Čerenkov material was lead glass SF–2 and the dimension was 300 mm cube. The density, radiation length, a reflective index for the D-line and critical energy are 3.85 g/cm³, 10.9 g/cm², 1.648 and 16.9 MeV, respectively. The Čerenkov light was collected on nine photomultipliers and their signals were added by a linear adder circuit. Output pulses from nine photomultipliers were adjusted in height and in time. The glass and photomultipliers were mounted in an iron box of 6 mm
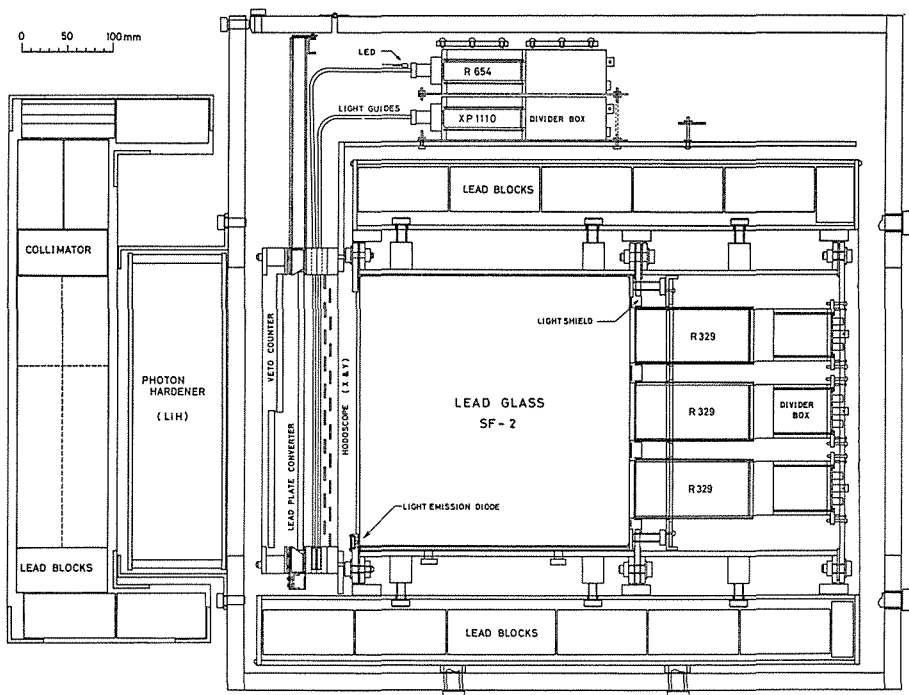

Fig. 6. The whole assembly of the photon detector for the measurement of a photon from the π°-meson.

thick.   A light emission diode was mounted on the lead glass to monitor the gain of photomultipliers.

The scintillator size of the hodoscope array was $3 \times 16 \times 302$ mm³.   The veto counter was separated into two scintillation counters.   Each scintillator was $153 \times 302 \times 6$ mm³ and overlapped 1 mm each other.

The whole assembly was shielded with lead blocks of 50 mm thick and mounted in an iron box of 19 mm thick.   A LiH absorber was placed to reduce the electro-magnetic background in front of the veto counters.   The thickness of LiH was 100 mm and the vessel was made of acrylite of 5 mm thick.

(b)   Calibration

The photon detector was calibrated up to 550 MeV by using mono-energetic electron beams which were analysed by the pair spectrometer.   The momentum spread of the electron beam was 1%.   The block diagram of the electronics is shown in Fig. 7.   Signals from the Čerenkov counter were splitted into two parts.   One was used for the fast coincidence with the pair counters (PAIR 1, PAIR 2 and PAIR 3) and triggered the linear gate circuit.   Another was fed to a small computer (OKITAC–4300) through the linear gate and analogue to digital converter (ADC) of CAMAC standard.   The pulse height distribution was displayed on a storage scope and
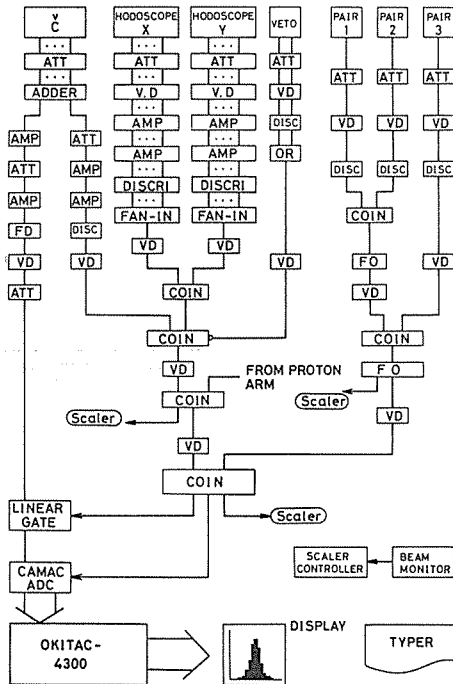

Fig. 7.   Block diagram of the electronics for the calibration of the photon detector.

punched out on a paper tape for an off-line analysis.   As is shown in Fig. 8, the energy resolution of the Čerenkov counter can be expressed as

$$\Delta E/E = 4.3 \times (E-30)^{-1/2}   \quad (E \text{ in MeV}),$$

when a lead plate of one radiation length was placed[22]~[24]. Detection efficiencies of the Čerenkov counter for electrons were also measured with different sets of the threshold level of the discriminator circuit as is shown in Fig. 9.
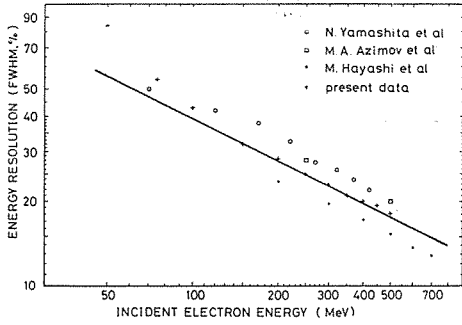
Fig. 8. Energy resolution of the Čerenkov counter. The lead plate converter of 5.8 mm thick was placed.
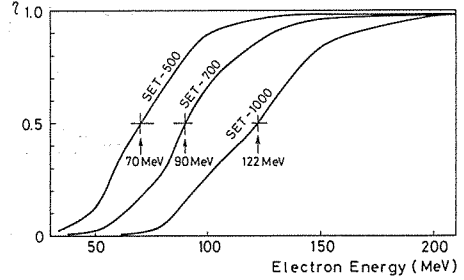
Fig. 9. Efficiency of the photon detector. The threshold level for each set was 70, 90 and 122 MeV, respectively.

II–5. Electronics and the on-line system

(a) Electronics

A block diagram and timing chart of the fast electronics were shown in Fig. 10 and Fig. 11, respectively.

Fig. 10. Block diagram of the electronics for the coincidence measurement of the reaction $\gamma p \rightarrow \pi^\circ p$. All accidental channel was not described.

Fig. 11.   Timing chart of the fast electronics.   The two signals presented in this chart show the
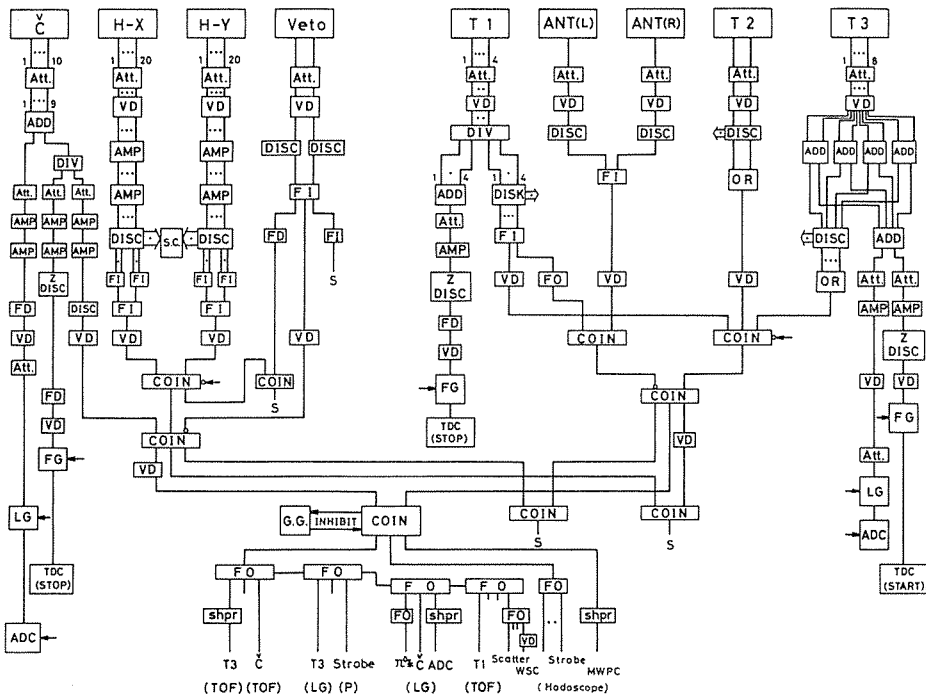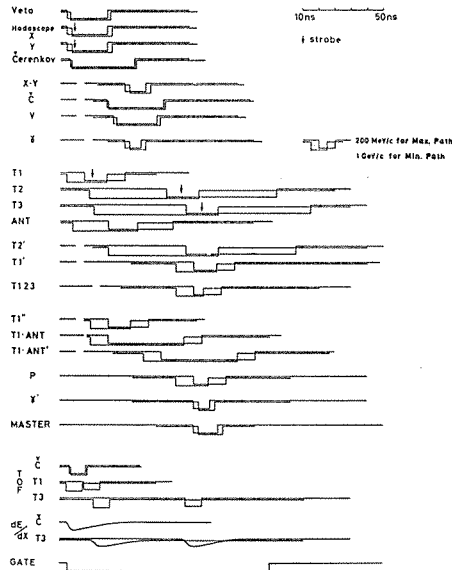timing of the signal due to the particle with minimum momentum for maximum path
and with maximum momentum for minimum path.

Logic of the gamma arm

Output signals of the Čerenkov counter were served as the Čerenkov signal ($\check{C}$).
They were splitted into three parts and were used as a logic signal, as an analogue
signal for pulse height analysis and as a stop signal for the measurement of the flight
time difference between the gamma arm and the proton arm.   Anyone of signals
from the hodoscopes for the vertical directions called X and those for the horizontal
direction called Y were fed into coincidence circuit (XY).   Anyone of signals from
the veto counters was called V.   Finally the coincidence signal ($XY \cdot C \cdot \overline{V}$) was
adopted as the γ signal.

Logic of the proton arm

Signals from T1, T2, T3 and ANTI were coincided ($T1 \cdot T2 \cdot T3 \cdot \overline{ANTI}$) and
adopted as the proton signal (P).   The coincidence width was chosen to be 80 ns to
detect the proton with the momentum ranged from 200 to 1000 MeV/c.

Signals from T1, T2 and T3 were fed to the strobed coincidence circuit to read
the bit informations of the each counter.   Signals from T1 and T3 counters were
used as the stop and start pulses for the measurement of the flight time of the particle.
Pulse heights of T3 (DE/DX) was used to identify the proton.

Double arm coincidence

A coincidence between gamma arm (γ) and proton arm (P) was made to identify
the reaction $\gamma p \rightarrow \pi^\circ p$ and used as the *MASTER* signal.   It triggered the high voltage
pulsing system of WSC, linear gate circuits, ADC, time to digital converter (TDC),
strobed coincidence circuits, MWPC and WSC read out systems.   When *MASTER*
signal was generated, the regeneration was inhibited for 20 m sec to provide enough
time to charge up the high voltage power supply of WSC.

(b) On-Line system

The block diagram of the on-line system is shown in Fig. 12. The following informations were stored in a small computer (TOSBAC–40C); pulse heights of the Čerenkov counter and T3 (DE/DX), flight time difference between the gamma arm and T3 (TOF–1), flight time between T1 and T3 (TOF–2), bit patterns of the hodoscope of the gamma arm, T1, T2 and T3, and the firing positions of MWPC and WSC. All informations for each event required 968 bits. The firing positions of MWPC and WSC were displayed on an oscilloscope of TOSBAC–40 event by event. These informations were sent to a central computer (TOSBAC–3400) by on-line and analysed in a real time. Each devices was monitored by the following distributions analysed by TOSBAC–3400; firing positions of MWPC, WSC, gamma hodoscope, T1, T2 and T3 and the pulse height of the Čerenkov counter. The distributions of TOF–1, TOF–2, DE/DX and the kinematical parameters such as K and θ_{π}^{cm} calculated by TOSBAC–3400 were sent back to TOSBAC–40 at the end of each run and printed out on a line printer. Finally, raw data were recorded on a magnetic tape for off-line analyses.
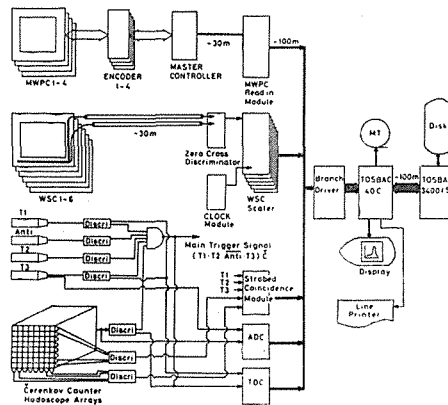
Fig. 12. Block diagram of the on-line system.

II–6. *Data Taking*

The set up parameters of the detection system were summarized in Table 1. The maximum energy of the bremsstrahlung was varied with the step of 100 MeV with the exception of the RUN (870–90). The magnetic field was adjusted to have a proper momentum acceptance according to each RUN. Usually the photon detector was set at 1132 mm apart from the target to get a high geometrical efficiency. When the counting rate of the veto counters become high, the photon detector was set at 1573 mm to reduce the accidental coincidence. The bias level of the Čerenkov counter was varied according to the counting rate and the momentum of a photon from a π°-meson. Each device was maintained to operate with a good condition by the informations described in the previous section.

Table 1. Set up parameters for each run. θ_p; set up angle of the magnetic spectro-
meter, Mag.; field strength of the analyzing magnet, θ_r; set up angles
of the photon detector, L_r; distances between the photon detector and
the target, Bias; threshold level of the photon detector.

RUN $(K-\theta_{\pi^0}^{cm})$ (MeV–deg.)	K^{max} (MeV)	θ_p (deg.)	Mag. (kG)	θ_r (deg.)	L_r (cm)	Bias (MeV)
700– 50	750	60.9	3.56	35.6	157.3	90
750– 60	850	57.4	4.65	43.1	113.2	90
700– 60	750	56.0	4.16	42.9	157.3	90
600– 60	650	56.0	3.95	44.3	157.3	90
500– 60	550	55.6	3.40	46.1	157.3	90
700– 70	750	51.1	5.15	53.0	157.3	90
600– 70	650	51.2	4.75	53.0	157.3	90
500– 70	550	51.0	3.97	54.0	157.3	70
650– 80	750	46.2	5.75	58.2	157.3	90
600– 80	650	46.3	5.13	60.4	113.2	90
500– 80	550	46.3	4.57	62.6	113.2	70
870– 90	1000	41.3	6.86	62.2	113.2	122
750– 90	850	42.1	4.82	66.3	113.2	90
700– 90	750	41.6	6.51	67.1	113.2	90
550– 90	650	41.6	5.75	69.2	113.2	90
450– 90	550	46.3	4.58	62.6	113.2	70
700–100	750	36.6	7.03	76.2	113.2	90
600–100	650	36.6	5.95	78.5	113.2	70
500–100	550	37.6	5.16	81.1	113.2	70
700–110	750	32.0	7.03	86.1	113.2	90
600–110	650	32.1	6.70	88.5	113.2	70
500–110	550	32.3	5.55	91.2	113.2	70
800–120	850	27.7	7.00	98.2	113.2	90
700–120	750	27.2	7.03	97.3	113.2	70
600–120	650	27.6	7.03	99.7	113.2	70
500–120	550	27.7	5.95	102.2	113.2	70
500–130	550	24.8	6.34	109.0	113.2	70

Chapter III.   Data Reduction

III–1.   General description

The differential cross sections were reduced from the event informations recorded
on the magnetic tape.   The flow chart of the data processing program is shown in
Fig. 13.   The four momentum of the recoil proton $(\vec{P}_p)$ was calculated from the
firing positions of MWPC, WSC and the magnetic field of the analysing magnet.
Kinematical parameters $(K, \theta_{\pi^0}^{cm}$ etc.) for the reaction $\gamma p \to \pi^0 p$ were reconstructed
from the $\vec{P}_p$.   The detection efficiencies of the whole detection system were evaluated
by the Monte Carlo method.

III–2.   Reduction of the proton momentum

(a)   MWPC fitting

The trajectory of protons from the target to the analysing magnet was determined
by the linear fitting method using the data of MWPC event by event.   Firstly, the
event with multiple firings in anyone of MWPC was rejected except the case where
neighbouring two or three wires were fired.   In that case the center of them was
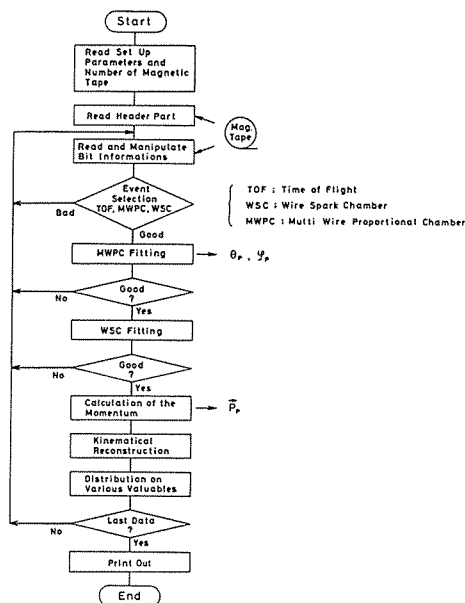
Fig. 13. Flow chart of the data processing program.

adopted as the firing position. Secondly, the event in which the deviation between the fired and the fitted position was greater than 5 mm this event was rejected. The full width at half maximum of the distribution of this deviation for good events was about 1.5 mm. The angle between the incident photon axis and the recoil proton (θ_p), and the injection angle to the analysing magnet (α) were determined by this fitted line.

(b) WSC fitting

The trajectory behind the analysing magnet was also determined by the linear fitting method using the WSC data. For each WSC, the data which gave the following characteristics were rejected from the fitting process; the multi-track, the fluctuation of the back fiducial count being greater than 0.1%, the difference between the fired and fitted position being greater than 3 mm. Finally, the event in which more than three of the WSC data were rejected by the reason above mentioned, were rejected. The full width at half maximum of the distribution of the deviation between the fired and fitted position was about 0.3 mm. The azimuthal angle (ϕ_p) and the ejection angle of the proton from the analysing magnet (β) was determined by this fitted line.

(c) Calculation of the proton momentum

The momentum of the proton (P_p^r) was calculated by the effective edge approximation and was represented in the following relation

$$P_P^r = \frac{0.3 \times B \times L}{\sin(\alpha) + \sin(\beta)},$$

where B is the strength of the magnetic field, L is the effective field length. The momentum of the recoil proton at the interacting point was given with

$$P_P = P_P^r + \delta P,$$

where δP is the momentum loss of the proton in the liquid hydrogen target, air and scintillators and other materials between the target and the magnet.   It was calculated from the range energy relation[25]. K and $\theta_{\pi^\circ}^{cm}$ were reconstructed from P_P, θ_P and ϕ_P.

III–3. Rejection of background events

Although the reaction $\gamma p \to \pi^\circ p$ was identified by the present coincidence measurement between the gamma arm and the proton arm, the distribution of TOF–1, TOF–2 and DE/DX were used to reduce the backgrounds due to other processes.   However, among the multi-pion production, the reaction $\gamma p \to \pi^\circ \pi^\circ p$ can contributes to the background of the present experiment.   This background was reduced to be less than 3% by choosing the events whose reconstructed energy of the initial photons laid between ($K^{max} - 250$ MeV) and K^{max}, where the K^{max} is the maximum energy of the bremsstrahlung.   The background due to the reaction $\gamma p \to \pi^+ n$ was negligibly small because of the coincidence measurement.

The reaction $\gamma p \to \gamma' p$ (proton Compton scattering) is very similar kinematically to the reaction $\gamma p \to \pi^\circ p$.   Moreover, the detection efficiency of the gamma arm for the former reaction is higher than that of the latter reaction.   In the present experiment, the fraction of the proton Compton events was determined from the distribution of the difference between the predicted and observed positions of a photon on the hodoscope of the gamma arm[26].   Assuming that the measured photons were produced by the proton Compton process, the predicted position of a photon on the hodoscope of the gamma arm was calculated using the momentum of a recoil proton measured with the proton arm.   The distributions of the difference between the predicted and measured positions are shown in Fig. 14.   The distributions of the difference thus obtained was simulated by the Monte Carlo calculation for the reaction
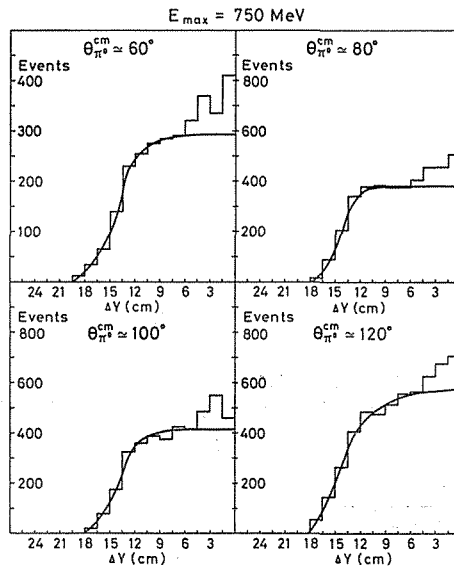

Fig. 14. Distribution of the difference between predicted and experimental position of a photon on the gamma hodoscope for the vertical direction (ΔY).   The peak around $\Delta Y=0$ are due to the events of the proton Compton process.

$\gamma p \to \pi^\circ p$ and is also shown in Fig. 14. The background due to the proton Compton process was estimated from this distributions and amounted from 3% to 30%.

III–4. *Monte Carlo simulation*

The detection efficiency and resolution of the whole detection system for the reaction $\gamma p \to \pi^\circ p$ was simulated by the Monte Carlo calculation. The block diagram of this calculation is shown in Fig. 15.
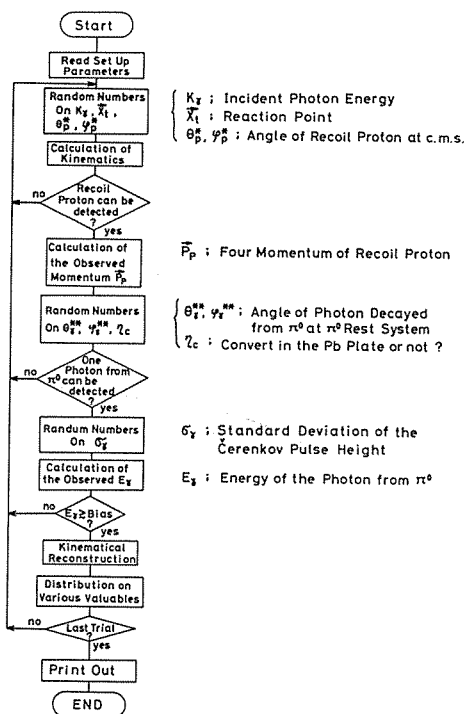

Fig. 15. Flow chart of the Monte Carlo program.

(a)   Random numbers on K_γ, $\vec{X}_t$, θ_p^{cm} and ϕ_p^{cm}

The energy spectrum of the incident photon was approximated by the Schiff's formula. The distribution of the reaction point $\vec{X}_t$ was assumed to be Gaussian for the radial and uniform along the beam axis. The standard deviation of the radial distribution was determined from the X-ray film exposed to the photon beam.

The distribution of $\cos \theta_p^{cm}$ and ϕ_p^{cm} were assumed to be uniform in this calculation, where θ_p^{cm} and ϕ_p^{cm} are the angle of the recoil proton in the center of mass system. The other kinematical parameters were calculated from K_γ, θ_p^{cm} and ϕ_p^{cm}.

(b)   Proton arm

The energy loss and multiple Coulomb scattering of the proton in the following materials were taken into account to reproduce the experimental condition; the liquid hydrogen target, Mylar of the target, MWPC and WSC, air, scintillators and wires.

(c)   Gamma arm

A π°-meson decays isotropically into two photons in the π° rest system. The

distribution of the random number on $\cos\theta_\gamma^{**}$ and ϕ_γ^{**} were assumed to be uniform, where θ_γ^{**} and ϕ_γ^{**} were the decay angle of the π°-meson in the π° rest system.

The following factors were calculated in the program; geometrical efficiency, conversion efficiency of a photon into electron-position pairs in the lead plate placed in front of the hodoscopes, attenuation factor of photons in the target and LiH absorber and counting losses due to discrimination of the electronics.

The conversion efficiency and attenuation factor were approximated by the following formula;

$$\eta_c = 1.0 - \exp\left(-\sigma\cdot\rho\cdot N\cdot x/A\right),$$

where ρ is the density of the material, N is the Avogadro number, A is the atomic number, x is the thickness of the material and σ is the cross section of the pair production. σ was calculated by the formula given by Sorensen[27], which was consistent with experimental results[28] within 1%. Fig. 16 shows energy dependence of the conversion efficiency and the attenuation factor.
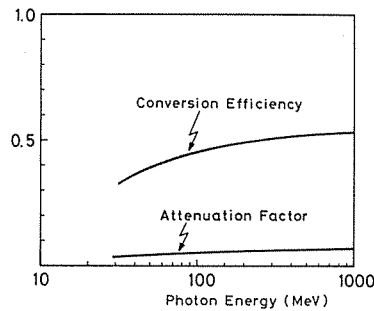

Fig. 16. Conversion efficiency of a photon in the lead plate of 5.8 mm thick and attenuation factor in the liquid hydrogen target and LiH absorber.

The energy distribution of photons in the lead glass was assumecd to be Gaussian, whose standard deviation was obtained from the result of the calibration run described in II–4. If the energy of photon was lower than the threshold level of the electronics, the event was rejected.

(d) Kinematical reconstruction

Kinematical parameters were reconstructed using observed values only on the event which could be detected. The procedure for the reconstruction of events was similar to the one for the experimental data. The difference between initial (generated) and simulated observables were also calculated. The distribution of these difference show the resolution of the detection system.

III–5. *Reduction of the differential cross section*

(a) Experimental yield

The experimental yield can be represented in the following relation;

$$Y_e = \frac{d\sigma}{d\Omega^*}d\Omega^*\cdot Q\cdot N_t\cdot\eta(\gamma,\,\mathrm{p})$$

with Y_e ;   coincidence rate of the photon from π°-meson and recoil proton of the reaction $\gamma\mathrm{p}\rightarrow\pi^\circ\mathrm{p}$,

$\dfrac{d\sigma}{d\Omega^*}$; differential cross section in the center of mass system,

Q ; number of incident photons,

N_t ; number of target protons,

$\eta(\gamma, \text{p})$; detection efficiency for the photon and proton,

$\eta(\gamma, \text{p})$ is given with

$$\eta(\gamma, \text{p}) = \eta(LiH) \cdot \eta(conv.) \cdot \eta(veto) \cdot \eta(bias) \cdot \eta(WSC) \cdot \eta(\text{p}).$$

$\eta(LiH)$ and $\eta(conv.)$ are the factors due to the attenuation of photons in the LiH absorber and the conversion of photons in the lead plate. $\eta(bias)$ is the loss of γ signals due to the discrimination of photons by electronics of the Čerenkov counter. The counting rate of the veto counter of the gamma arm was very high ($\sim 5 \times 10^9$ sec^{-1}) when it was placed near the beam line and target. Then the accidental coincidence between the veto counter and the other counter was recorded on a scaler circuit. The loss of γ signal due to this reason [$\eta(veto)$] was summarized in Table 2. The loss of the *MASTER* signals [$\eta(WSC)$] during the inhibited time was measured and is also listed in Table 2. $\eta(\text{p})$ is the loss of the recoil protons in the proton arm due to energy loss, multiple scattering and the nuclear absorption. The loss due to the nuclear absorption in the scintillation counter was estimated to be less than 2%. The loss due to the energy loss and multiple scattering were taken into account in the Monte Carlo calculation.

The accidental coincidence between the gamma and proton arm was amounted to 0.6~5.7% for the almost all experimental set up as listed in Table 2. On the other hand, the time resolution of MWPC and WSC were not so good in comparison with the scintillation counter system. Therefore, the trajectories of multi particles were recorded in MWPC and WSC accidentally. The ratio of the events which satisfied the criteria of reconstructions in III–2, to the total events ranged from 63% to 89%. The correction factor [η_r] due to this reason was given by the following relation,

$$\eta_r = \frac{N_r}{N(1-r)},$$

where N_r is the number of events satisfied the criteria, N is the number of total events and r is the ratio of the accidental coincidence to the total events. The results were also listed in Tabl 2.

The counting rate with the empty target was less than 0.5% of the one with the full target and we neglect this correction.

Q is given with

$$Q = \frac{1}{K^{\max}} \int K \frac{B(K)}{K} dK = \frac{U}{K^{\max}}$$

where $B(K)$ is the spectral function of bremsstrahlung and U is the total energy of incident photons measured with the thick walled ionization chamber. Fig. 17 (a)~ (d) show the distributions of the experimental yield normalized by the equivalent quanta.

(b) Monte Carlo yield and cross sections

The Monte Carlo yield can be expressed in the following formula,

Table 2. Normalization corrections and the rate of the accidental coincidence. η(Veto) is the inefficiency due to the accidental coincidence between the veto counter and the other counters, η(WSC) is the inefficiency due to the inhibited time of the MASTER signal and η_r is the reconstruction efficiency.

RUN ($K-\theta_{\pi^0}^{cm}$)	η (Veto)	η (WSC)	Accidental Coincidence	η_r
(MeV–deg.)	(%)	(%)	(%)	(%)
700– 50	4.7	4.3	9.3	82.3
750– 60	5.7	5.9	3.3	90.3
700– 60	2.3	2.8	1.4	86.8
600– 60	2.7	2.8	3.8	86.0
500– 60	1.9	1.9	1.7	86.0
700– 70	1.9	4.3	4.1	63.8
600– 70	1.9	2.8	3.0	83.2
500– 70	1.2	2.8	0.6	87.0
650– 80	1.5	6.8	4.8	93.4
600– 80	1.6	3.5	5.7	82.1
500– 80	4.4	3.1	2.4	85.3
870– 90	3.9	12.4	2.8	77.2
750– 90	4.9	20.0	1.8	80.5
700– 90	6.5	11.6	4.7	83.2
550– 90	1.3	10.0	5.0	84.9
450– 90	2.0	7.0	0.8	83.7
700–100	1.6	8.7	4.6	87.6
600–100	1.7	8.2	1.7	85.4
500–100	1.8	7.8	1.4	85.8
700–110	1.2	10.1	1.2	80.2
600–110	1.3	8.7	1.7	79.4
500–110	1.4	8.0	1.8	79.2
800–120	1.1	8.2	1.5	64.2
700–120	1.0	9.3	1.6	76.9
600–120	0.7	5.4	1.0	79.0
500–120	0.7	6.2	1.0	78.1
500–130	0.7	5.4	1.7	67.5

$$Y_m = \int d\Omega^* \cdot Q_m \cdot \eta_m(\gamma, p) \cdot \alpha_m^{-1}$$

with Y_m ; Monte Carlo yields,

Q_m ; number of photons generated in the simulation,

$\eta_m(\gamma, p)$; detection efficiency taken into account in the simulation described in III–4 with

$\eta_m(\gamma, p) = \eta_m(LiH) \cdot \eta_m(conv.) \cdot \eta_m(bias) \cdot \eta_m(p)$,

α_m ; correction factor due to the restriction of the angle θ_p^{cm} and θ_p^{cm} to increase the Monte Carlo efficiency.

Q_m is given with

$$Q_m = \frac{C}{K^{max}} \int K \frac{B(K)}{K} dK,$$

where C is the normalization constant and is expressed with

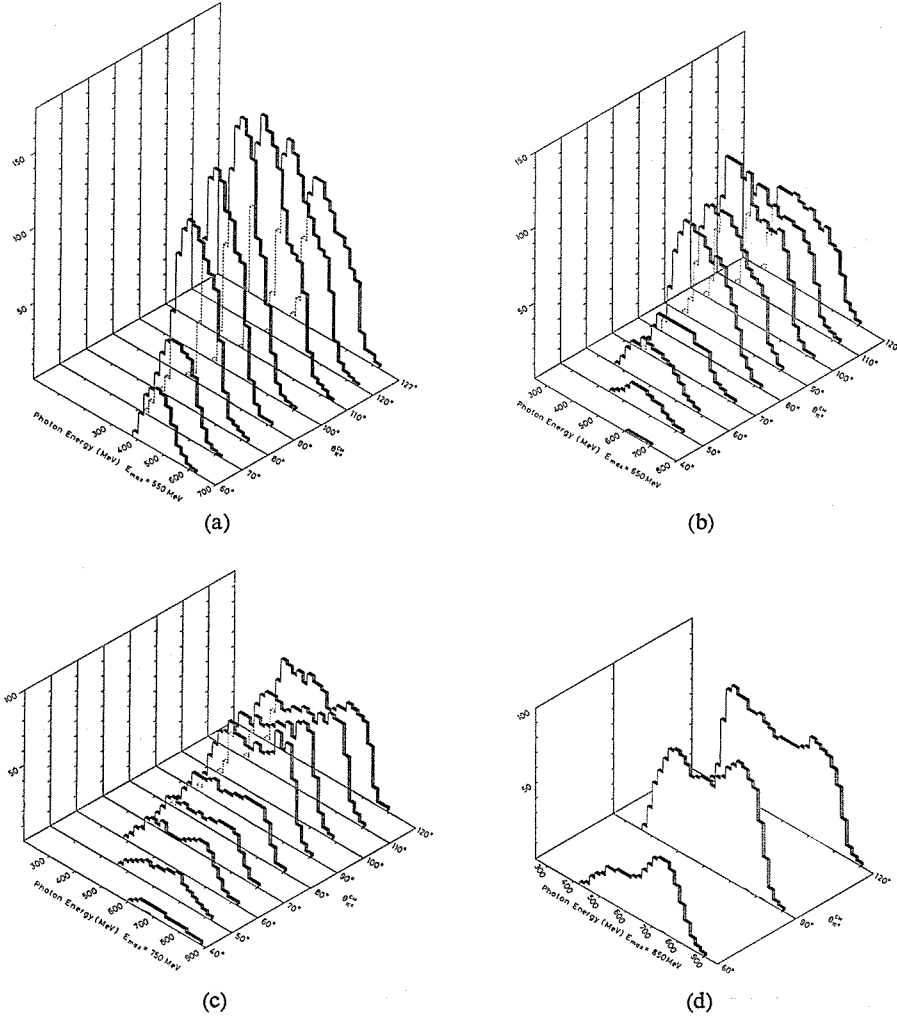$$C = \frac{M_t}{\int_{K^1}^{K^2} \frac{B(K)}{K} dK}$$

Fig. 17. Experimental yield as a function of the incident photon energy and $\theta_{\pi^\circ}^{cm}$, where E_{max} is the maximum energy of the bremsstrahlung.

(a) $E_{max} = 550$ MeV, (b) $E_{max} = 650$ MeV, (c) $E_{max} = 750$ MeV and (d) $E_{max} = 850$ MeV.

with M_t is the total trial number is the simulation, K^1 and K^2 is the minimum and maximum energies of the incident photon generated in the simulation, respectively.

Finally, the differential cross section can be expressed with

$$\frac{d\sigma}{d\Omega^*} = \frac{Y_e}{Q}\left(N_t \cdot \frac{Y_m}{M_t} \cdot \alpha_m \frac{\int_{K^1}^{K^2} \frac{(BK)}{K} dK}{\frac{1}{K^{max}} \int K \frac{B(K)}{K} dK}\right)^{-1}$$

Chapter IV.   Experimental Results

The present results $(d\sigma/d\Omega^*)$ on the differential cross sections are summarized

in Table 3.   The resolutions for the incident photon energy ΔK and for the $\pi°$-c.m. angle $\Delta\theta_{\pi°}^{cm}$ are expressed in the following relations;

$$\Delta K=\left(\left(\frac{\partial K}{\partial P}\Delta P\right)^2+\left(\frac{\partial K}{\partial\theta_p}\Delta\theta_p\right)^2\right)^{1/2}$$

$$\Delta\theta_{\pi°}^{cm}=\left(\left(\frac{\partial\theta_{\pi°}^{cm}}{\theta_p}\Delta P\right)^2+\left(\frac{\partial\theta_{\pi°}^{om}}{\partial\theta_p}\theta_p\right)^2\right)^{1/2}$$

where ΔP and $\Delta\theta_p$ are the momentum and the angular resolution of the magnetic spectrometer calculated by the Monte Carlo method as described in III-4.   These resolutions are summarized in Table 4 for each data point.   The energy step between the data points was not chosen to be equal to the energy resolution.   The energy resolution is about the same as the energy step at angles greater than 90°.   However at the forward angles, the energy resolution becomes rather wider than the energy step.   The angular acceptance of each data point was ranged from 3° to 4° (FWHM). The angular resolution of the detection system is almost better than the angular acceptance.

Table 3.   Differential cross sections for the reaction $\gamma p\rightarrow\pi°p$, obtained by the coincidence measurement with the magnetic spectrometer and the photon detector.   The presented errors include only statistical errors.

K (MeV)	$\theta_{\pi°}^{cm}$ (deg.)	$d\sigma/d\Omega*$ (μb/sr)
	50°	
610	53.5	1.90±0.12
630	53.0	1.89±0.12
650	53.0	1.96±0.12
670	53.0	1.88±0.11
690	53.0	1.84±0.11
	60°	
490	64.0	5.29±0.32
510	63.5	4.25±0.26
530	63.5	3.49±0.22
550	63.5	3.05±0.20
570	63.5	2.61±0.18
590	63.0	2.33±0.16
610	61.0	1.98±0.05
630	61.0	1.98±0.05
650	61.0	2.11±0.05
670	60.5	2.31±0.05
690	60.5	2.66±0.05
710	60.5	2.96±0.05
730	60.5	3.02±0.05
750	60.0	3.00±0.05
	70°	
450	73.0	8.17±0.34
470	73.0	6.70±0.28
490	73.0	5.64±0.24
510	72.0	4.16±0.20

Table 4.   Resolutions of the present experiment at each data point. ΔK is the energy resolution of the incident photon and $\Delta\theta_{\pi°}^{cm}$ is the angular resolutions of the $\pi°$-angle in the center of mass system.

K (MeV)	ΔK (FWHM) (MeV)	$\Delta\theta_{\pi°}^{cm}$(FWHM) (deg.)
$\theta_{\pi°}^{cm}=$ 50°		
610	84	4.1
630	83	4.0
650	85	3.9
670	87	3.8
690	87	3.7
$\theta_{\pi°}^{cm}=$ 60°		
490	57	4.1
510	57	4.0
530	57	3.8
550	59	3.6
570	59	3.5
590	60	3.3
610	60	3.2
630	62	3.1
650	62	3.0
670	62	2.8
690	63	2.7
710	64	2.6
730	64	2.6
750	65	2.5
$\theta_{\pi°}^{cm}=$ 70°		
450	41	3.8
470	42	3.6
490	42	3.4
510	42	3.2

K (MeV)	$\theta_{\pi^o}^{cm}$ (deg.)	$d\sigma/d\Omega^*$ (μb/sr)	K (MeV)	ΔK (FWHM) (MeV)	$\Delta\theta_{\pi^o}^{cm}$(FWHM) (deg.)
530	73.5	3.66 ± 0.31	530	44	3.0
550	73.5	3.28 ± 0.28	550	44	2.9
570	73.5	2.56 ± 0.24	570	45	2.7
590	73.5	2.56 ± 0.24	590	46	2.6
610	73.0	2.73 ± 0.19	610	46	2.5
630	73.0	2.81 ± 0.19	630	47	2.4
650	73.0	2.84 ± 0.19	650	47	2.3
670	73.0	2.79 ± 0.18	670	47	2.2
690	73.0	2.71 ± 0.18	690	47	2.2
	80°		$\theta_{\pi^o}^{cm}=$ 80°		
410	83.0	$12.9\ \pm0.42$	410	33	3.6
430	83.0	$10.7\ \pm0.35$	430	33	3.3
450	83.0	8.60 ± 0.29	450	34	3.1
470	83.0	7.03 ± 0.25	470	34	2.9
490	83.0	5.81 ± 0.21	490	35	2.7
510	83.0	4.83 ± 0.18	510	36	2.6
530	83.0	3.94 ± 0.17	530	36	2.5
550	83.0	3.88 ± 0.16	550	36	2.4
570	83.0	3.38 ± 0.14	570	37	2.3
590	83.0	2.70 ± 0.12	590	37	2.2
610	83.0	2.98 ± 0.18	610	37	2.1
630	83.0	2.77 ± 0.17	630	37	2.0
650	83.0	3.00 ± 0.17	650	38	1.9
670	83.0	2.95 ± 0.16	670	38	1.9
	90°		$\theta_{\pi^o}^{cm}=$ 90°		
390	92.0	$15.3\ \pm0.50$	390	28	3.3
410	92.0	$11.9\ \pm0.39$	410	28	3.1
430	92.0	$10.0\ \pm0.33$	430	28	2.8
450	91.5	7.63 ± 0.27	450	29	2.6
470	91.5	6.78 ± 0.24	470	29	2.5
490	91.5	5.63 ± 0.22	490	28	2.3
510	91.5	5.54 ± 0.22	510	29	2.2
530	93.5	4.89 ± 0.31	530	29	2.1
550	93.0	4.05 ± 0.27	550	30	2.0
570	93.0	3.16 ± 0.23	570	30	1.9
590	93.0	3.15 ± 0.22	590	31	1.8
610	93.0	2.79 ± 0.18	610	31	1.8
630	93.0	2.77 ± 0.17	630	28	1.7
650	90.5	3.26 ± 0.09	650	27	1.7
670	90.5	3.40 ± 0.09	670	31	1.6
690	90.0	3.82 ± 0.09	690	32	1.6
710	90.0	4.29 ± 0.09	710	32	1.5
730	90.0	4.35 ± 0.09	730	32	1.5
750	90.0	4.55 ± 0.10	750	32	1.4
770	90.0	4.17 ± 0.10	770	32	1.4
790	91.5	3.99 ± 0.12	790	33	1.4
810	91.0	3.56 ± 0.11	810	33	1.3
830	91.0	3.09 ± 0.10	830	33	1.3
850	91.0	2.67 ± 0.09	850	33	1.3
870	91.0	2.19 ± 0.08	870	34	1.2
	100°		$\theta_{\pi^o}^{cm}=$100°		
390	102.5	$16.6\ \pm0.63$	390	24	2.9

Table 3. (Continued)

K (MeV)	$\theta_{\pi^0}^{cm}$ (deg.)	$d/\sigma d\Omega^*$ (μb/sr)
410	102.0	13.2 ±0.51
430	102.0	10.7 ±0.44
450	102.0	8.69±0.37
470	101.0	7.69±0.34
490	101.0	5.55±0.28
510	103.0	4.71±0.26
530	103.0	4.74±0.27
550	102.0	4.09+0.24
570	102.0	3.76±0.23
590	103.2	3.77±0.22
610	102.0	3.02±0.19
630	103.5	3.65±0.21
650	103.0	3.08±0.19
670	102.0	3.61±0.20
690	102.0	3.62±0.20
	110°	
390	113.5	14.5 ±0.49
410	113.0	11.9 ±0.42
430	113.0	9.76±0.35
450	112.5	7.18±0.28
470	112.0	5.27±0.24
490	112.0	4.71±0.22
510	111.5	4.53±0.21
530	113.0	4.17±0.21
550	112.0	3.54±0.18
570	112.0	3.54±0.17
590	112.0	2.90±0.16
610	112.0	2.53±0.15
630	112.0	2.50±0.14
650	111.5	2.21±0.13
670	111.5	2.44±0.14
690	111.5	2.35±0.13
	120°	
390	123.5	12.6 ±0.50
410	123.0	9.69±0.40
430	123.0	7.56±0.34
450	122.5	6.38±0.30
470	122.0	5.42±0.26
490	123.5	4.77±0.24
510	123.0	4.48±0.18
530	123.0	3.78±0.19
550	122.5	3.24±0.16
570	122.0	3.10±0.16
590	121.5	2.46±0.14
610	121.5	2.26±0.13
630	122.0	2.61±0.15
650	120.0	2.79±0.07
670	120.0	2.79±0.07
690	120.0	2.86±0.07
710	120.0	3.25±0.07
730	120.0	3.22±0.07
750	119.5	3.15±0.07

Table 4. (Continued)

K (MeV)	ΔK (FWHM) (MeV)	$\Delta\theta_{\pi^0}^{cm}$ (FWHM) (deg.)
410	25	2.6
430	25	2.5
450	25	2.3
470	25	2.2
490	26	2.1
510	26	1.9
530	26	1.9
550	26	1.8
570	26	1.7
590	27	1.6
610	27	1.6
630	27	1.5
650	27	1.5
670	27	1.4
690	27	1.4
$\theta_{\pi^0}^{cm}=110°$		
390	22	2.6
410	21	2.4
430	22	2.2
450	23	2.1
470	23	1.9
490	23	1.8
510	23	1.7
530	20	1.7
550	23	2.3
570	23	1.5
590	23	1.5
610	23	1.4
630	23	1.4
650	24	1.3
670	24	1.3
690	24	1.2
$\theta_{\pi^0}^{cm}=120°$		
390	20	2.3
410	20	2.2
430	20	2.0
450	20	1.9
470	21	1.8
490	21	1.7
510	20	1.6
530	21	1.5
550	21	1.5
570	21	1.4
590	21	3.1
610	21	1.3
630	21	1.2
650	21	1.2
670	22	1.2
690	22	1.1
710	23	1.1
730	23	1.0
750	24	1.0

K (MeV)	$\theta_{\pi^0}^{cm}$ (deg.)	$d\sigma/d\Omega^*$ (μb/sr)	K (MeV)	ΔK (FWHM) (MeV)	$\Delta\theta_{\pi^0}^{cm}$ (FWHM) (deg.)
770	119.5	3.03±0.07	770	25	1.0
790	119.5	2.80±0.07	790	26	1.0
	130°		$\theta_{\pi^0}^{cm}=130°$		
410	130.0	9.57±0.48	410	19	2.0
430	129.0	7.61±0.40	430	19	1.9
450	128.5	6.00±0.34	450	19	1.8
470	128.5	5.40±0.31	470	19	1.7
490	128.5	4.66±0.27	490	19	1.6
510	128.0	3.60±0.23	510	19	1.5

The errors listed in Table 3 include only the statistical errors. However there are the following origins of the systematic error.

1) The uncertainties due to the maximum energy of the bremsstrahlung ($\Delta K^{max}/K^{max}$) were about 0.5%, because the beam spill was kept to be about 4 m sec during the experiment.

2) The uncertainty of the number of target protons due to evaporating of the liquid hydrogen was estimated to be less than 1.0%.

3) The total energy of the incident photon beam was measured by the thick walled ionization chamber. The total energy U is represented with

$$U = \alpha_i \cdot \alpha_c,$$

where α_i is the calibration constant of the current integrator and α_c is the calibration constant of the thick walled ionization chamber, whose error were 1.3% and 2.0%, respectively.

4) The uncertainties of the efficiency of the gamma arm was considered as follows. The cross section of pair production in the material was calculated as described in III–4(c). It is consistent with the experimental value within 1.0%. The threshold level of the Čerenkov counter was measured frequently during the experiment and their fluctuation was less than 0.3%. The geometrical efficiency of the gamma arm was defined by the hodoscope. The pulse height of the Čerenkov counter for the photon entered in the edge of the counter become smaller than that for the photon entered in the central region because of the leakage of the electromagnetic shower from the lead glass. The error due to this origin was estimated to be negligibly small.

5) The ambiguity caused by the Monte Carlo calculation of the momentum acceptance and the solid angle of the proton arm was the most heavy source of the systematic error. The detection efficiencies at the border of the acceptance were fall steeply against the proton momentum or angles. Therefore, we adopt only the central region of the acceptance for each experimental set up, where the efficiencies varied smoothly. The error due to this origin was estimated to be less than 5.0%.

6) The error in estimating the fraction of proton Compton events was almost less than 1.0%, but it was mounted to 2.0% at 60° and 5.0% at 50°.

7) The other factors of the uncertainties such as $\eta(veto)$, $\eta(WSC)$ and η_r were less than 1.0%.

The quadrature sum of these systematic errors amount to be 5.9% at angles between 70° and 130°, and 6.2% at 60° and 7.7% at 50°.
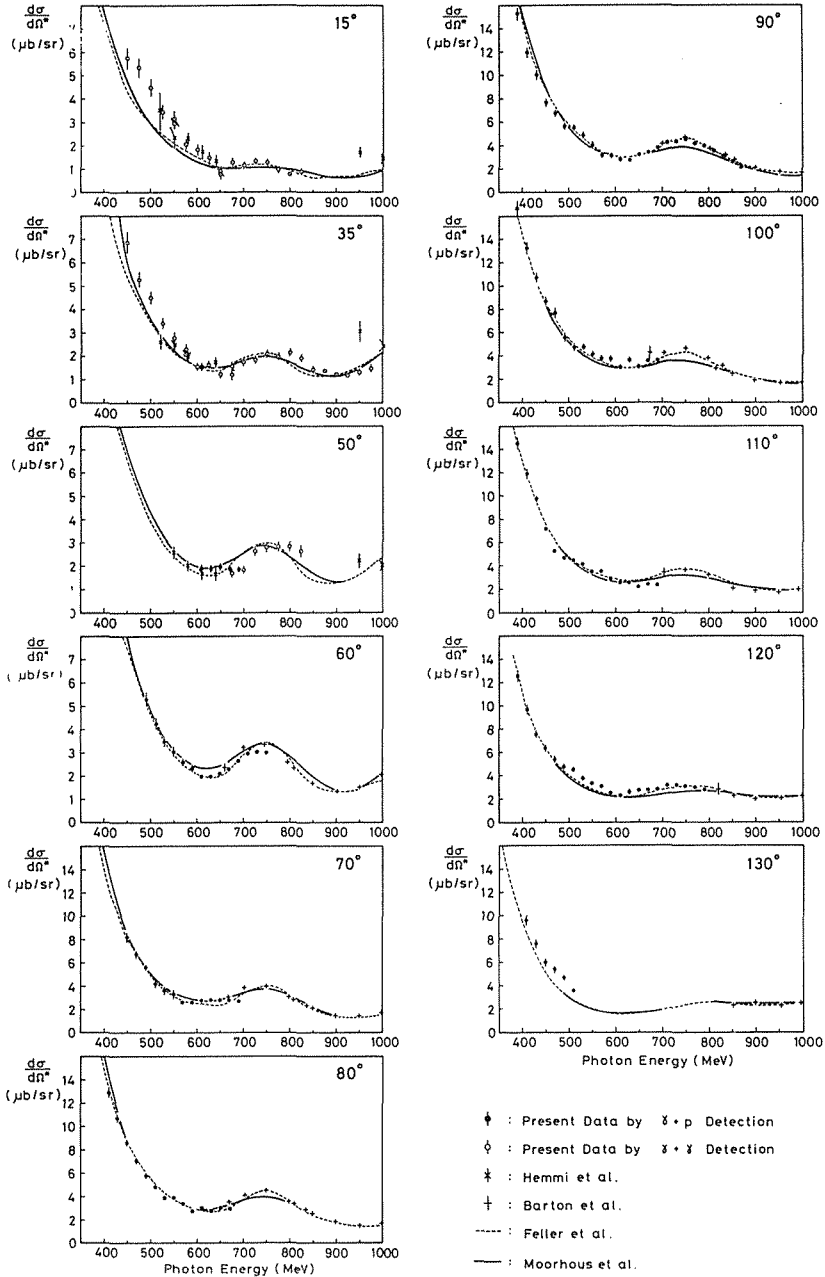
Chapter V.   Discussions

Fig. 18.   The energy dependence of the differential cross sections for the reaction $\gamma p \rightarrow \pi^\circ p$.   The solid and dashed curves are from partial wave analyses by NAGOYA and MOR, respectively. ϕ; represents the present results obtained by the coincidence measurement with the magnetic spectrometer and the photon detector, ϕ; the present results obtained by the π°-detector, $*$; Y. Hemmi et al., $\dagger$; J. S. Barton et al.

The energy dependence of the cross sections between 15° and 130° are plotted in Fig. 18 and Fig. 20 (a)~(k) together with the results obtained with the $\pi°$ detector at forward angles. The recent results obtained at other laboratories[13),14),29)~36)] are also plotted in these figures. The data noted by the open circles were the results
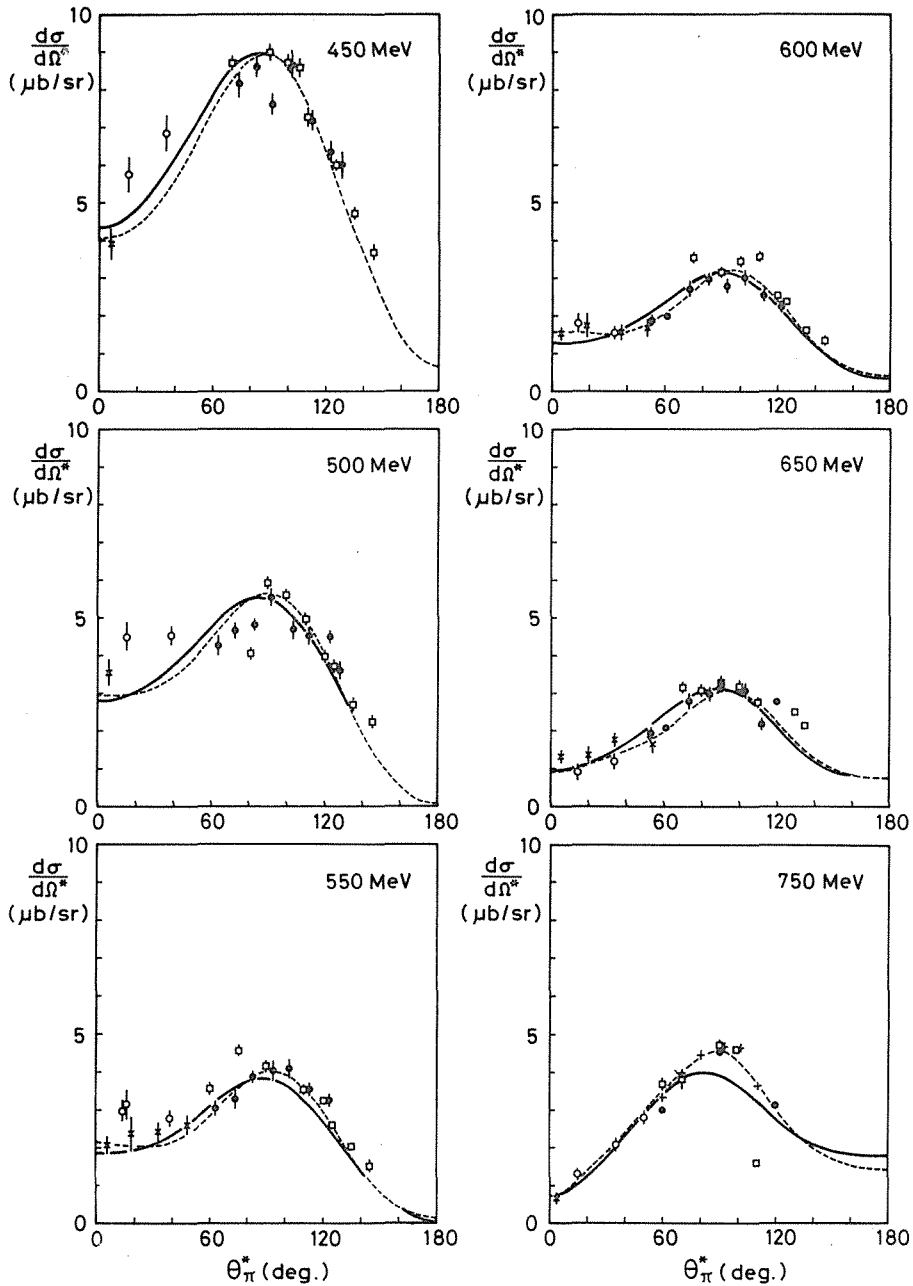
Fig. 19. The angular dependence of the differential cross sections for the reaction $\gamma p \rightarrow \pi°p$. ⊟ represents the results by P. Dougan et al. The other notations are the same in Fig. 18.

obtained with the $\pi°$ detector.   Fig. 19 shows the angular distributions at the energies between 450 and 750 MeV.   The results obtained by the two different detection systems were overlapped at the angle of 50° between 600 and 750 MeV.   They show a fairly good agreement with each other.   Systematic errors caused by the beam properties, the liquid hydrogen target and the beam monitor were the same in these results because of the simultaneous measurements.

In the energy region below 490 MeV, present results were overlapped with the combined data of experiments carried out at the 500 MeV electron synchrotron at Bonn University[31),32),34)].   They measured the differential cross sections by detecting only the recoil protons using the magnetic spectrometer or the range telescope.   The consistency of their results were very well.   The agreement of the present results with theirs is seen to be almost good.   Our experimental region overlaps widely with the one by Dougan et al.[13),14)].   They also detected only the recoil protons by the range telescope.   Our results were consistent with them at the angle of 50°, 80°, 90°, 100° and 120°, but there are some discrepancies at the angle of 60° and 110°.   In the energy region above the second resonances, present results were overlapped with the results by Feller et al.[33)], Barton et al.[30)] and Booth et al.[35)] at the angle of 60°, 90° and 120°.   Feller et al. detected only the recoil proton with the magnetic spectrometer.   In these single arm experiments, the backgrounds due to proton Compton processes can not be rejected in the experiments.   Barton et al. detected the recoil protons with the range telescope in coincidence with the one of the photons from the $\pi°$-meson.   However, the Compton backgrounds were not eliminated in the measurement.   Therefore, they made a correction using the Compton differential cross sections which is not well established by the experiments.   Booth et al. also detected the recoil proton and the photon and subtructed the Compton processes by the method nearly the same as the present experiment.   In these coincidence experiment, the contamination due to the reaction $\gamma p \rightarrow \pi^+ \pi^- p$ and $\gamma p \rightarrow \pi^+ n$ is negligibly small as described in III–4.   The present results at the angle of 60° are somewhat smaller than the other ones.

There are few experiments at the forward angles ($\theta_\pi^{cm} \leq 50°$) with the exception of Hemmi et al.[29)] in this energy range.   They are well agree between the first and second resonance region, but there are discrepancies at the energy of 950 MeV.

The solid and dashed curves in Fig. 18 and Fig. 19 represent the predicted value by MOR and NAGOYA, respectively.   The solid curves in Fig. 20 are the predicted value by MW.   The results by MW and NAGOYA have the same feature concerned with the differential cross section.   In comparing these predicted value with the present results, following discussions can be made.   In the angular range from 60° to 110°, the fit by MW is better than the fit by MOR.   The predicted value by MOR
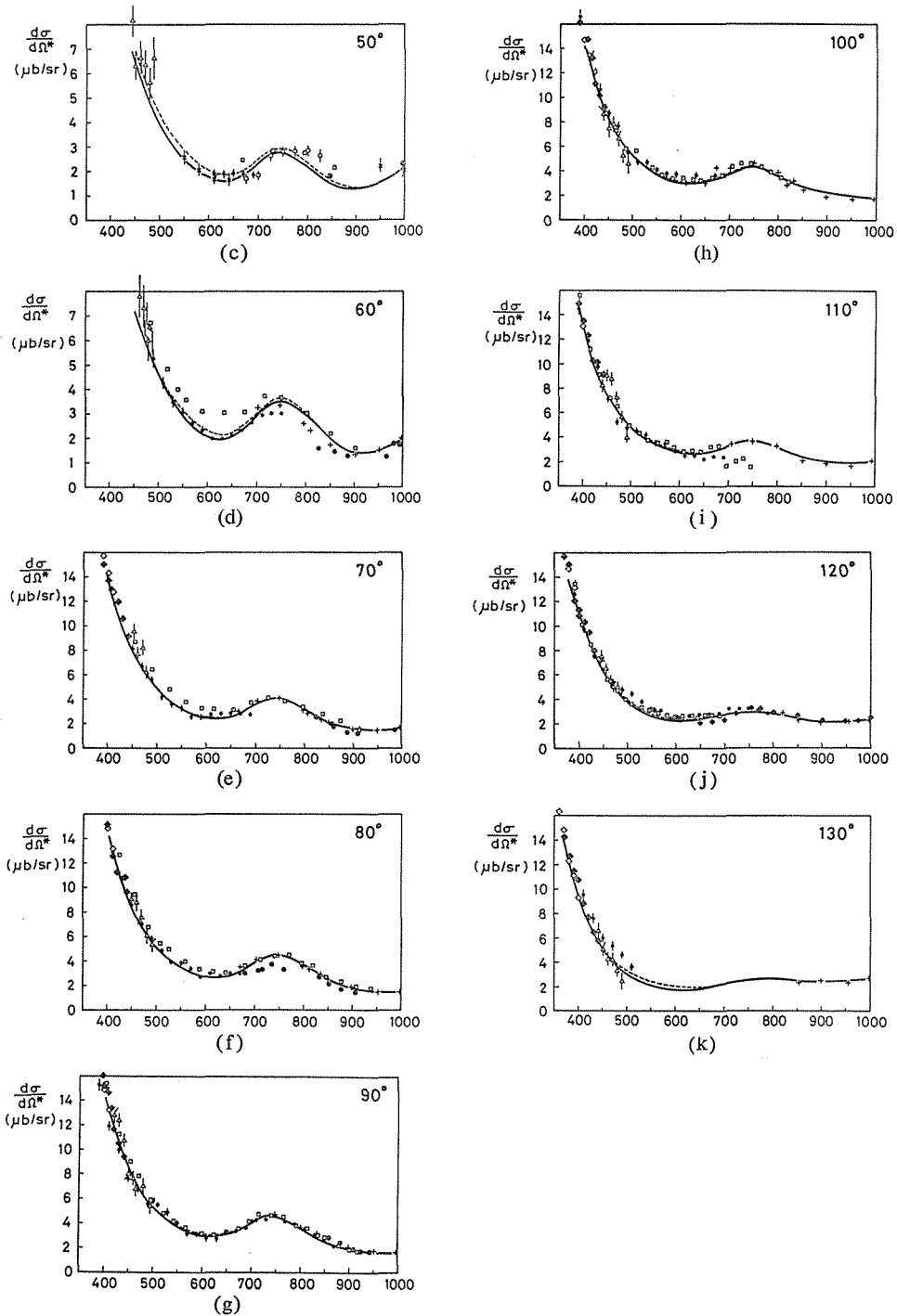

(a)   (b)
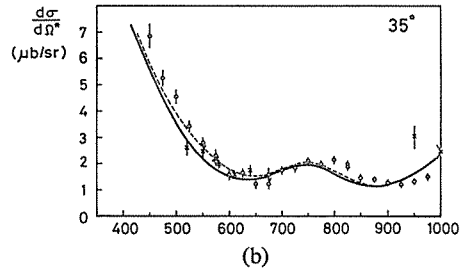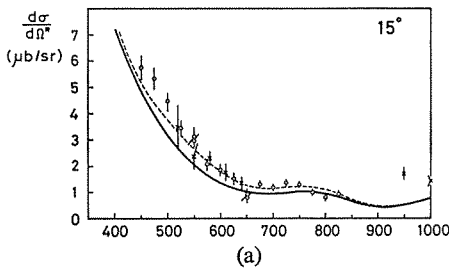
Fig. 20(a)~(i). The energy dependence of the differential cross sections for the reaction $\gamma p \rightarrow \pi^\circ p$. $\diamondsuit$; G. Fischer et al., $\oplus$; W. Braunschweig et al. $\blacklozenge$; P. Feller et al., $\varDelta$; H. Genzel, $\oplus$; P. S. L. Booth et al.[35] and $\odot$; P.S.L. Booth et al.[36]. The solid curves are from partial wave analysis by MW. The dashed line are the results of modified partial wave analysis of MW at the present work.

are too small around the second resonances near 90°.   The present results are higher than both analyses at the forward angles and backward angles (15°, 35°, 120° and 130°) below 600 MeV.

Using the s-channel helicity amplitudes in the notation of Walker[3], the differential cross section in single pion photoproduction of nucleons can be given by

$$\frac{d\sigma}{d\Omega} = \frac{1}{2} \frac{q}{k} \sum_{i=1}^{4} |H_i|^2$$

with

$$H_1 = \frac{1}{\sqrt{2}} e^{i\phi} \sin\theta \cos\frac{1}{2}\theta \sum_{n=1}^{\infty} (B_{n+} - B_{(n+1)-})(P''_n - P''_{n+1}) ,$$

$$H_2 = \sqrt{2} \cos\frac{1}{2}\theta \sum_{n=0}^{\infty} (A_{n+} - A_{(n+1)-})(P'_n - P'_{n+1}) ,$$

$$H_3 = \frac{1}{\sqrt{2}} e^{2i\phi} \sin\theta \sin\frac{1}{2}\theta \sum_{n=1}^{\infty} (B_{n+} + B_{(n+1)-}))P''_n + P''_{n+1}) ,$$

$$H_4 = \sqrt{2} e^{i\phi} \sin\frac{1}{2}\theta \sum_{n=0}^{\infty} (A_{n+} + A_{(n+1)-})(P'_n + P'_{n+1}) ,$$

where k and q are the momenta of photons and nucleons in the c.m. system, respectively, P'_l and P''_l are derivatives of Legendre polynominals. H_1 and H_3 are the initial-helicity-3/2 amplitudes and H_2 and H_4 are the initial-helicity-1/2 amplitudes. $A_{l\pm}$ and $B_{l\pm}$ are the helicity element corresponding to the state with pion orbital angular momentum l and total angular momentum $j = l \pm 1/2$. H_2 and H_4 are the amplitudes which do not vanish at the forward and backward angles, respectively. In order to improve the fit at forward and backward angles by modifying the MW analysis, the helicity elements $A_{l\pm}$ must be changed.   The largest amplitude of $A_{l\pm}$ below 600 MeV is the resonant amplitude of $P_{33}(1236)$.   By modifying the resonance parameter of $P_{33}(1236)$, a better fit can be obtained in our energy region.   However, at the energy around the first resonance, the fit gives very large χ^2.   And then, we modified only the background amplitude to explain these characteristics of the present results.   The input value of the $Re(A_{1+})$ of the reaction $\gamma p \to \pi° p$ was changed at the

Table 5.   (a) The input value of the background partial wave $Re(A_1^+)$ of the reaction $\gamma p \to \pi° p$.   The units are $\mu b^{1/2}$.

	K (MeV)	525	700	850
Re (A_{1+}) ($\gamma p \to \pi° p$)	Original Metcalf-Walker	−0.144	−0.114	−0.100
	Modified	−0.25	−0.20	−0.16

(b) χ^2/(number of data).

$\theta_{\pi°}^{cm}$	χ^2/(no. of data)	
	Metcalf-Walker	Modified
15°	3.59	1.86
35°	3.61	2.29
120°	3.36	2.07
130°	4.40	3.20
all data	2.47	2.19

energy of 525, 700 and 850 MeV as listed in Table 5 (a). Other helicity elements were not changed.

In this modification, the major constraint of MW's model, that the background amplitude should vary smooth with energy, is ensured. Other observables such as $P(\theta)$, $T(\theta)$ and $\Sigma(\theta)$ are scarcely changed by this modification. The fitted curves are shown in Fig. 20 by the dashed line. $\chi^2/$(number of data) are listed in Table 5 (b). It is clear that our modification can reproduce our results at the forward and backwark angles and give smaller values for χ^2. Our results indicate that the MW's resonance amplitudes can reproduce the experimental results on the reaction $\gamma p \rightarrow \pi^\circ p$ below 1 GeV and are seemed to be established in this energy region. However, it is needed to understand the background amplitudes by the experimental and theoretical efforts such as double polarization measurements and analysis basing on the dispersion relation.

ACKNOWLEDGEMENT

REFERENCES

1) R. Marshall, Raporter talk in the International Symposium on Lepton and Photon Interactions at High Energies (DESY, 1977).
2) T. Nakamura and K. Ukai, INS, Internal Report, INS–TH–116 (1977). The world data of the single pion photo-production were compiled in a magnetic tape.
3) R. L. Walker, Phys. Rev. 182 (1969) 1729.
4) W. J. Metcalf and R. L. Walker, Nucl. Phys. B76 (1974) 253.
5) P. Feller, M. Fukushima, N. Horikawa, R. Kajikawa, K. Mori, T. Nakanishi, T. Ohshima, C. O. Pac, M. Saito, S. Suzuki, Y. Tarui, T. Yamaki, T. Matsuda, K. Mizushima and N. Tokuda, Nucl. Phys. B104 (1976) 219.
6) P. Feller, M. Fukushima, N. Horikawa, R. Kajikawa, K. Mori, T. Nakanishi, T. Ohshima, c. O. Pac, M. Saito, S. Suzuki, Y. Tarui, T. Yamaki, T. Matsuda, K. Mizushima and N. Tokuda, Nucl. Phys. B102 (1976) 207.
7) G. Knies, R. G. Moorhouse and H. Oberlack, Phys. Rev. D9 (1974) 2680.
8) R. G. Moorhause, H. Oberlack and A. H. Rosenfeld, Phys. Rev. D9 (1974) 1.
9) R. C. E. Devenish, D. H. Lyth and W. A. Rankin, Phys. Lett. 52B (1974) 227.
10) D. Faiman and A. W. Hendry, Phys. Rev. 180 (1969) 1572.
11) L. A. Copley, G. Karl and E. Obryk, Phys. Lett. 29B (1969) 117.

12) R. P. Feynman, M. Kislinger and R. Ravndal, Phys. Rev. **D3** (1971) 2706.

13) P. Dougan, T. Kivikas, K. Lungner, V. Ramsay and W. Stiefler, LUND, Internal Report, LUSY 7502 (1975).

14) P. Dougan, V. Ramsay and W. Stiefler, LUND, Internal Report, LUSY 7504 (1975).

15) K. Gomi and H. Fujii, Private communication.

16) A. Imanishi, S. Kato, K. Shiino, T. Toshioka, K. Ukai, K. Watanabe, M. Daigo, Y. Hemmi, R. Kikuchi, M. Minowa, K. Miyake, T. Nakamura, A. Noda, M. Ono, Y. Suzuki, M. Yoshioka, M. Chiba, K. Sugano, T. Shimomura, T. Shinohara and Y. Hoshi, Submitted to Nucl. Instr. and Meth. (1977).

17) M. Chiba, M. Daigo, S. Kato, K. Kondo, K. Toshioka and K. Watanabe, Japan. J. appl. Phys. **15** (1976) 1135.

18) Y. Hoshi, T. Shimomura, M. Yoshioka and K. Watanabe, INS, Internal Report, INS–TH–106 (1976), (in Japanese)

19) G. Charpak, D. Rahm and H. Steiner, Nucl. Instr. and Meth. **80** (1970) 13.

20) K. Watanabe and T. Shimomura, INS, Internal Report, INS–TH–104 (1976), (in Japanese).

21) S. Kato, K. Sugano and M. Yoshioka, INS, Internal Report, INS–TH–102 (1975).

22) N. Yamashita, Ph. D. Thesis, Memoirs of the Faculty of Science, Kyoto University, Series A, **35** (1977) 35.

23) M. A. Azimov, V. S. Pantujev and M. N. Khachaturyan, Nucl. Instr. and Meth. **39** (1966) 325.

24) M. Hayashi, S. Homma, N. Kajiura, T. Kondo and S. Yamada, Nucl. Instr. and Meth. **94** (1966) 297.

25) M. Rich and R. Madey, UCRL–2301 (1954).

26) K. Toshioka, M. Chiba, S. Kato, K. Sugano, K. Ukai, T. Shimomura, T. Shinohara, M. Daigo, Y. Hemmi, R. Kikuchi, M. Minowa, K. Miyake, T. Nakamura, A. Noda, M. Ono, Y. Suzuki, M. Yoshioka and Y. Hoshi, INS, Internal Report, INS-Report-294 (1977).

27) A. Sorenssen, Nuovo Cimento **38** (1965) 745; Ibid. **41** (1966) 543.

28) T. Miyachi, A. Akino, K. Gomi, A. Kusumegi, M. Mishina, H. Okuno, I. Sato, M. Takeda and M. Yoshioka, J. Phys. Soc. Japan **33** (1972) 577; Ibid. **34** (1973) 14.

29) Y. Hemmi, T. Inagaki, Y. Inagaki, A. Maki, K. Miyake, T. Nakamura, N. Tamura, J. Tsukamoto, N. Yamashita, H. Itoh, S. Kobayashi, S. Yasumi and H. Yoshida, Phys. Lett. **43B** (1973) 79.

30) J. S. Barton, P. S. L. Booth, L. J. Carroll, J. R. Holt, J. N. Jackson, G. Moscati and J. R. Wormald, Nucl. Phys. **B84** (1975) 449.

31) G. Fischer, H. Fischer, G. von Holtey, H. Kampgen, G. Knop, P. Schuiz and H. Wessels, Z. Physik **245** (1971) 225.

32) W. Barunschweig, H. Genzel and R. Wedemeyer, Z. Physik **245** (1971) 253.

33) P. Feller, H. Herr, E. Hilger, V. Kadansky, D. Menze, Th. Miczaila, U. Opara and W. J. Schwille, Phys. Lett. **49B** (1974) 197.

34) H. Genzel, Z. Physik **268** (1974) 37.

35) P. S. L. Booth, M. F. Butler, L. J. Carrol, J. R. Holt, J. N. Jackson, W. H. Range, E. G. H. Williams and J. R. Wormald, Nuovo Cimento **13A** (1973) 235.

36) P. S. L. Booth, L. J. Carrol, J. R. Holt, J. N. Jackson, W. H. Range, K. A. Sprakes and J. R. Wormald, Nucl. Phys. **B84** (1975) 435.